Optical Metrology of the Optical Communications Telescope Laboratory 1-Meter Telescope by Means of Hartmann Tests Conducted at the Table Mountain Observatory

A. H. Vaughan[1] and D. Mayes[2]

This article describes the use of a pupil mask and a charge-coupled device (CCD) camera with stellar sources to characterize the optical performance of a 1-meter telescope, built for JPL by the firm Brashear LP of Pittsburgh, Pennsylvania, after the telescope was permanently installed in JPL's Optical Communications Telescope Laboratory (OCTL) at the Table Mountain Observatory. A total of twenty-two 1-minute exposures of a 6th magnitude star were recorded over a span of 1 hour on the night of June 3, 2004, UTC. "Seeing" was estimated at 1 arcsecond or better. Analyzed by methods described herein, the method yields Zernike wavefront aberration coefficients having an average standard deviation of about ±0.04 wave at 633 nm per individual frame for the low-order aberrations considered (x-tilt, y-tilt, defocus, X-astigmatism, T-astigmatism, x-coma, and y-coma). The formal standard deviation of the mean, estimated by dividing by $\sqrt{(N-1)}$, where $N = 22$ frames, thus approaches ±0.01 wave. This compares favorably with the accuracy achieved by interferometry in factory tests of the OCTL telescope. The root-sum-square (rss) sum of astigmatism and coma is shown to be in the neighborhood of 0.13 wave root-mean-square (rms). Of this total, about 0.09 wave rms is due to coma that could, in principle, be corrected by re-centering the secondary by 0.002 inch (50 μm).

I. Introduction

A reliable way to characterize the wavefront produced by an optical system is through the use of the classical Hartmann test [1,2], in which the paths of light "rays" defined by holes in a mask are deduced from measurements of their intercepts with planes at known axial distances from the paraxial focus. The test can make use of time exposures of adequate duration to make it relatively insensitive to random disturbances caused by atmospheric turbulence and tracking jitter. The method thus readily lends itself to the testing of large-aperture optics and to optical testing in the presence of vibration and atmospheric turbulence. In tests of an astronomical or tracking telescope, the light source can be any star of suitable

[1] Space Experiments Systems Section, JPL retiree contracted through Chipton-Ross, Inc., El Segundo, California.

[2] Earth Sciences Section.

The research described in this publication was carried out by the Jet Propulsion Laboratory, California Institute of Technology, under a contract with the National Aeronautics and Space Administration.

brightness. The classical Hartmann method is simpler than the so-called Shack–Hartmann test often used for wavefront sensing in adaptive optics systems. In Shack–Hartmann, an image of the system pupil is formed on an array of small lenses (a micro-lens array), serving to form an array of star images on a detector. The classical form of the Hartmann test uses no optical components other than those under test, except for the mask, whose pertinent dimensions are readily National Institute of Standards and Technology (NIST)-traceable.

The classical Hartmann test introduces an accurately known pupil intensity function (the mask with circular holes) having symmetrical spatial features of known size and locations. Each hole in the mask defines a bundle of rays that samples a specific sub-aperture of the pupil. Diffraction may or may not contribute significantly to the out-of-focus image structure in a Hartmann test (depending upon wavelength and upon the geometrical placement of the detector intercepting the rays). Because diffraction by a circular aperture is symmetrical, the centroids of light bundles passing through them can be assumed to define ray paths that can be accurately described in terms of geometrical optics. The precise path of a given bundle of rays depends sensitively upon the surface slope errors on the optical elements that may exist at the particular sub-aperture sampled. The position at which the centroid of a given ray intercepts a known plane (the surface of a charge-coupled device (CCD) used as the detector), compared to the intercept of a ray centered on the same sub-aperture point as predicted for a perfect optical system by ray tracing, serves to measure the net optical surface slope error encountered by the ray in question. The statistical analysis of the ensemble of slope errors serves to characterize the optical quality of the system and the influences of atmospheric turbulence. Alternatively, as will be described, the ensemble of time-averaged slope errors can be fitted by a least-squares procedure to spatial derivatives of Zernike wavefront functions representing wavefront aberrations of the system.

II. Basic Approach

Although the 1-meter-diameter primary mirror serves as the entrance stop of the Optical Communications Telescope Laboratory (OCTL) telescope, a Hartmann mask is more conveniently located external to the telescope, slightly in front (skyward) of the secondary mirror. For tests limited to on-axis field points, this is practically equivalent to placement of the mask at the primary mirror, but it avoids the potential complication of light traversing the mask in two directions (before and after reflection in the primary); and the mounting of the mask is more easily managed. Our mask was fabricated by means of precision water-jet machining of 1/4-inch ($\sim$0.6 cm) paper-sandwiched Styrofoam ("art board"), chosen both for its dimensional stability and its light weight, avoiding the need to re-balance the telescope in accommodating the mask. The mask contains a rectangular pattern of 20 evenly spaced holes (not counting a center hole), the holes representing essentially equal area fractions of the pupil. Subsequent to the observations described in this article, the mask hole pattern was subjected to validation at the JPL Measurement Assurance Center using a Brown & Sharpe Coordinate Measuring Machine. Mask dimensional errors (computed from measurements at eight points around the perimeter of each hole) were found to be small in comparison to the telescopic aberrations of interest (see Discussion, Section VII).

For the observations reported here, the mask was approximately centered on the aperture as judged by eye to avoid vignetting (exact centering is not required for a mask located in the collimated light of object space of a well corrected telescope). The mask was clocked in such a way as to avoid obscuring any of its holes by secondary mirror support vanes.

To allow the out-of-focus images to fill a convenient format on our detector (an Apogee® 1056×1024 CCD array of 14 μm pixels), the detector was located (in two successive series of tests) at two different positions Δ, determined to be 36.65 inches (93.09 cm) and 25.40 inches (64.52 cm) beyond the paraxial coudé F/75 focus of the telescope. The hole diameter d was chosen to minimize the size of the blur circle caused by the combination of defocus and diffraction. This occurs when the two contributions are made approximately equal, so that

$$d = f \cdot \sqrt{\frac{2.44 \cdot \lambda}{\Delta}} \approx 96.8 \cdot \mathrm{mm}$$

where $f = 75,000$ mm is the nominal F/75 coudé focal length, and $\lambda = 632$ nm is taken to be the effective wavelength. The blur circle size at the detector (the root-sum-square (rss) of defocus and diffraction blur in equal amounts) is then approximately

$$2.44 \cdot \sqrt{2} \cdot \lambda \cdot \frac{f}{d} \approx 1.7 \cdot \mathrm{mm} \approx 113 \cdot \mathrm{pixels}$$

The spacing between the holes (and hence the number of holes in the Hartmann screen) was chosen to separate the blur circles in the plane of the detector by approximately the blur circle diameter, avoiding cross talk between adjacent spots that might influence the determination of spot centroids. The resulting mask layout is shown to scale in Fig. 1.

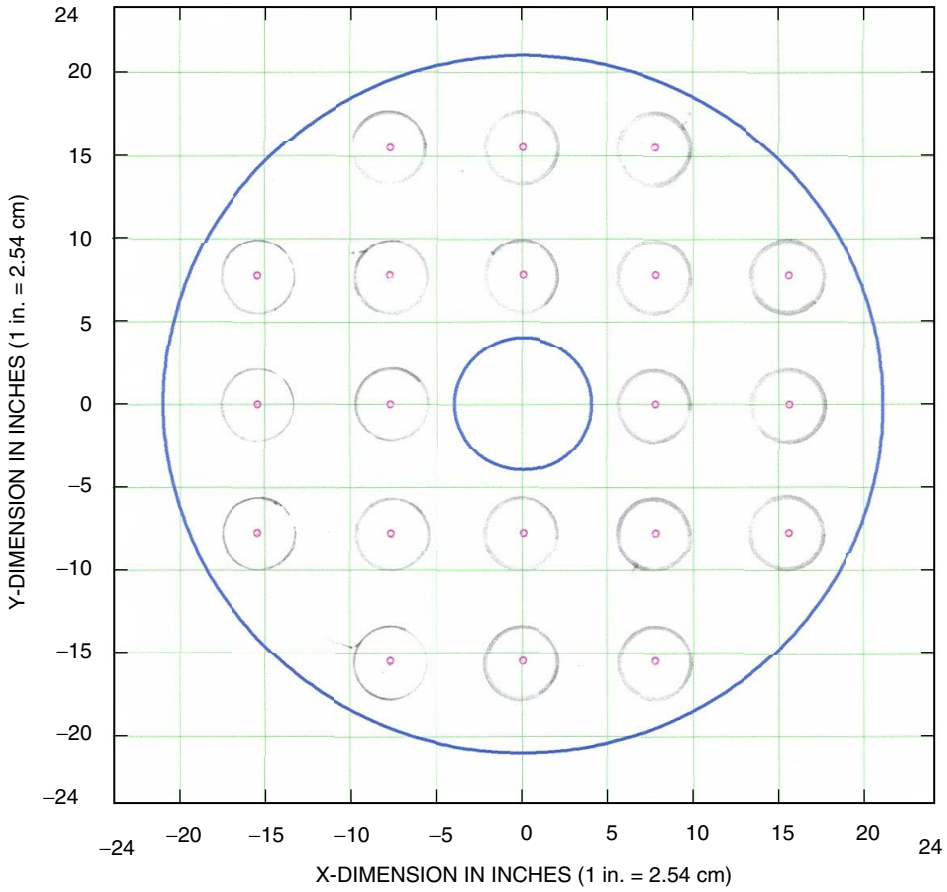

Fig. 1. The Hartmann mask layout, with dimensions shown in inches. Holes lie on 7.75-inch (19.68-cm) centers to an estimated precision of about 0.005 inch (13 μm). Hole diameters are 3-13/16 inches (9.68 cm). The outside diameter of the mask is 42 inches (107 cm). Optimal hole size was calculated to minimize spot blur sizes at the location of our detector, which was about 36 inches (91.44 cm) beyond the paraxial coudé focus of the telescope. The mask was fabricated by water jet machining of 1/4-inch- (0.635 cm)-thick art board.

Experience has shown that a good centroiding algorithm can estimate the position of the centroid of an approximately Gaussian star image to an accuracy of about 1 percent of its diameter, in this case about 17 μm, or 1.1 pixels. Considering the lever arm of 75 meters + Δ, the corresponding rms accuracy for estimation of wavefront slope error is (17 μm)/(75.9) = 2.2×10^{-7} radians. Extended across an aperture radius of 50 cm, this slope measuring error would give a peak-to-valley wavefront error of about 0.18 wave at 633 nm. One might naively expect that, for $N = 20$ spots, the overall peak–valley measuring error would be reduced by a factor $1/\sqrt{(N-1)}$, to be of order 0.04 wave. If, as in the present case, a total of 22 such independent measurements (frames) are combined by averaging, the resulting standard deviation of the mean might be expected to approach 0.01 wave, assuming the errors involved are entirely random. These crude estimates are in fact not far from the reproducibility of measurement actually achieved, as will be described.

III. The Observations

In preparation for the tests reported here, steps were taken to ensure the stablest possible operating conditions in the OCTL dome. Thus, the dome was opened at evening twilight and remained open under ambient conditions for about 2 hours prior to the beginning of our tests. Before attaching the Hartmann mask to the telescope, we confirmed the approximate position of the optical axis by pointing the telescope at a bright star and visually bore sighting from the coudé focus to verify centration of the beam within the clear apertures of the secondary mirror and intervening five plane fold mirrors along the coudé light path. We concluded that our estimated location of the optical axis was accurate to within approximately 15 arcseconds (5.5 mm), as compared to the telescope's design half-field of view of 126 arcseconds (46 mm). Using the CCD camera, we confirmed the approximate axial location of the plane of best focus from which to measure focus offsets Δ. Finally, by trial, we established that at the focus offsets of interest, exposures of 1-minute duration using a 6th magnitude star (FK5 #1339) would give a useful exposure level with adequate time averaging of the effects of atmospheric turbulence.

A total of 22 frames were recorded over a 1-hour time span (05:30 to 06:25 UTC), during which the star's elevation decreased from 67.8 to 57.3 degrees above the horizon. Two independent series of test exposures were made, hereinafter called Series 1 (frames 39 through 50 at the shorter defocus distance) and Series 2 (frames 54 through 64 at the longer defocus distance). Typical exposures (frames 39 and 54) belonging to Series 1 and Series 2, respectively, are shown in Fig. 2.

IV. Estimation of Centroids

The critical data needed in Hartmann testing consist of suitably accurate measurements of the CCD pixel coordinates of the centroids of the recorded blur circles or spots. Our analysis using computer-simulated data suggested that a positional accuracy of about 1 pixel rms (or one percent of the blur diameter of a spot) would be necessary as well as sufficient to achieve a precision of 0.01 to 0.02 rms wave at 633 nm in the determination of low-order Zernike wavefront aberrations for the OCTL telescope. Various centroiding methods were considered [4], all making use of initial approximate estimates of images recorded in the Flexible Image Transport System (FITS) format. Approximations made by eye, from inspection of images as displayed on a monitor, were estimated to have a precision of two or three pixels. Because the "eye" is very good at judging centroids while disregarding artifacts such as dust particle shadows, such approximations were retained as "sanity checks" on more refined methods. We adopted a quadrant-sensor algorithm that we deemed sufficiently accurate while requiring only about 30 seconds of computation for each set of 20 spot images in a CCD frame. To each spot image, a cutoff was imposed at a radial distance (from the eye-estimated centroid) large enough to include most of the light in a Hartmann spot image, but small enough to exclude light from the wings of adjacent spots. To further improve the accuracy of the method, we replaced all "hot pixel" intensity readings by the average of the four neighboring pixels in each row and column. We believe our centroid determinations closely approach the 1-pixel accuracy level, so that measuring errors are not an important factor in the interpretation of our results.

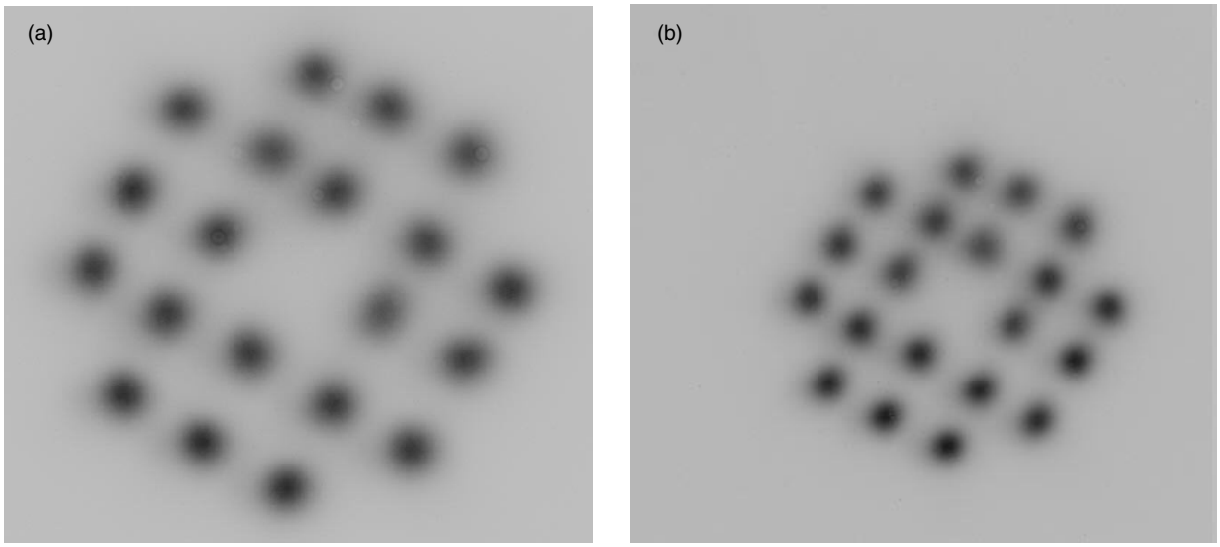

Fig. 2. Negatives of Hartmann test frames (a) 39 from Series 1 and (b) 54 from Series 2, made with an Apogee CCD camera spaced about 93.09 cm and 64.52 cm, respectively, from the paraxial focus. Frame sizes are 1056 × 1024 pixels. Measured centroid coordinates of the 20 blurred spots in each frame are used to derive geometrical image patterns and Zernike wavefront aberration coefficients, as described in the text.

V. Interpretation of Centroid Data

The simplest method of interpreting the centroid data from a Hartmann test is to project each ray bundle (represented by a ray extending from the center of the corresponding hole in the screen) to its intercept in the plane of best focus so as to create a spot diagram. Two pre-processing steps are executed at this stage. First, the origin of the (x,y)-centroid coordinates is shifted to the center of the spot pattern. Second, a coordinate rotation about the origin in the (x,y)-plane is performed to align the spot pattern with the hole pattern in the mask, so as to minimize the rms spread of points in the resulting spot diagram. In the case of the OCTL, a slightly different, monotonically changing degree of rotation is required for each successive frame because of field rotation in the coudé system. In this way, we develop for each frame a geometrical spot diagram consisting of 20 ray intercepts, representing the geometrical performance of the telescope with atmospheric turbulence largely averaged out over the 1-minute duration of an exposure. A typical spot diagram obtained in this way is shown in Fig. 3. The resulting rms geometrical spot radii from analysis of all 22 frames are listed in the second column ("Spot") of Table 1 (for Series 1) and Table 2 (for Series 2). The rms spot radii average 0.36 and 0.37 arcsecond, respectively. The standard deviations among frames was 0.07 to 0.08 arcsecond. These results are model-independent, assuming only the laws of geometric optics.

To derive the wavefront errors, we make explicit use of the fact that the Hartmann test measures slope errors. The slope errors are determined from the difference between the observed detector coordinates (ξ_{obs}, η_{obs}) of the centroid of a blur circle and the position $(\xi_{calc}, \eta_{calc})$ predicted by scaling the Hartmann screen pattern to the size it would occupy in the plane of the detector for the appropriate value of Δ (use of the scaled pattern is equivalent to ray tracing a perfect optical system). The wavefront slope errors ΨX_i and ΨY_i in the x- and y-directions, respectively, at the location of the ith hole are given in radians by

$$\Psi X_i = \frac{\xi_{i,obs} - \xi_{i,calc}}{f + \Delta}$$

$$\Psi Y_i = \frac{\eta_{i,obs} - \eta_{i,calc}}{f + \Delta}$$

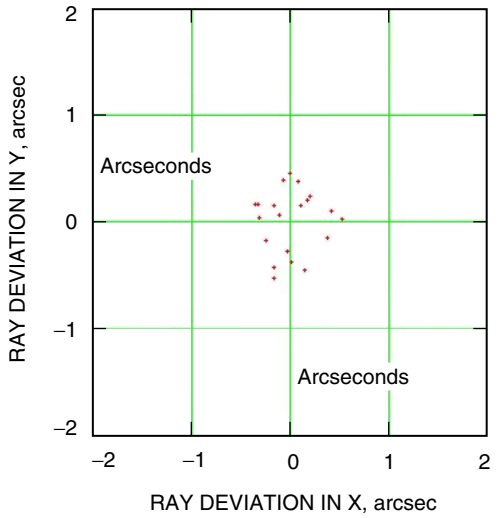

Fig. 3. Geometrical spot diagram derived from a single Hartmann test frame by tracing rays from the Hartmann mask to their intercept at the detector, and extending the rays to the plane of best focus (minimum rms scatter). The Hartmann pattern is centered and de-rotated in pre-processing, as described in the text. Seeing effects are largely (although not entirely) averaged out in the 1-minute exposures used in this investigation.

The x- and y-components of wavefront slope errors are given by first derivatives of the Zernike polynomials. The first eight of these are given for reference in Table 3, where we make use of the Zernike Standard Polynomials defined in ZEMAX [3]. Since the Zernike polynomials are defined only within a circle of unit radius, the pupil coordinates x and y in these expressions are assumed to be normalized to the unit circle.

In the present application, we have omitted spherical aberration for two reasons: (1) factory acceptance tests of the OCTL telescope showed that this aberration is negligibly small compared to other aberrations; and (2) we deemed that a Hartmann mask containing only 20 holes would not provide adequate sampling to reliably distinguish spherical aberration from defocus.

The x- and y-components of total wavefront slope error at the ith hole position are represented by

$$SX_i = \sum_{j=1}^{m} a_j \cdot \frac{\partial J_j(x_i, y_i)}{\partial x}$$

$$SY_i = \sum_{j=1}^{m} b_j \cdot \frac{\partial J_j(x_i, y_i)}{\partial x}$$

where m is the number of terms used. We seek to choose coefficients a_j and b_j in such a way as to minimize

Table 1. Results for frames 39 through 50.

(1) Frame number	(2) Spot	(3) x-tilt	(4) y-tilt	(5) Defocus	(6) X-astigmatism	(7) T-astigmatism	(8) x-coma	(9) y-coma
39	0.313	−0.128	0.161	−0.012	0.039	0.023	−0.066	0.079
40	0.283	−0.094	0.076	0.016	0.056	0.026	−0.014	0.065
41	0.258	−0.077	0.112	−0.038	0.065	−0.011	−0.050	0.064
42	0.307	−0.059	0.132	0.006	0.056	0.026	−0.037	0.056
43	0.281	−0.047	0.138	0.026	0.035	0.025	−0.052	0.042
44	0.301	−0.118	0.143	0.001	0.045	0.029	−0.045	0.073
45	0.274	−0.085	0.133	0.016	0.047	0.033	−0.043	0.052
46	0.341	−0.089	0.209	0.017	0.095	0.041	−0.089	0.050
47	0.307	−0.095	0.173	−0.024	0.057	0.025	−0.065	0.063
48	0.263	−0.079	0.123	−0.003	0.066	0.031	−0.045	0.051
49	0.377	−0.051	0.270	0.005	0.111	0.029	−0.142	0.023
50	0.399	−0.075	0.264	0.016	0.155	0.041	−0.138	0.051
Average all frames	0.309	−0.083	0.161	0.002	0.069	0.026	−0.065	0.056
Standard deviation	0.044	0.024	0.059	0.019	0.035	0.013	0.039	0.015
Standard of the mean	0.013	0.007	0.018	0.006	0.011	0.004	0.012	0.004
Average frames 39–44	0.291	−0.087	0.127	0.000	0.049	0.020	−0.044	0.063
Standard deviation	0.020	0.032	0.030	0.023	0.011	0.015	0.017	0.013
Standard of the mean	0.009	0.014	0.013	0.010	0.005	0.007	0.008	0.006
Average frames 45–50	0.327	−0.079	0.195	0.005	0.089	0.033	−0.087	0.048
Standard deviation	0.055	0.016	0.063	0.016	0.040	0.006	0.044	0.013
Standard of the mean	0.025	0.007	0.028	0.007	0.018	0.003	0.208	0.006
Difference frames (39-44) − (45-50)	−0.036	−0.008	−0.068	−0.005	−0.040	−0.014	0.043	0.015

Table 2. Results for frames 54 through 64.

(1) Frame number	(2) Spot	(3) x-tilt	(4) y-tilt	(5) Defocus	(6) X-astigmatism	(7) T-astigmatism	(8) x-coma	(9) y-coma
54	0.343	−0.101	0.059	−0.020	0.143	0.041	−0.049	0.046
55	0.416	−0.181	0.178	0.003	0.227	0.010	−0.072	0.087
56	0.354	−0.076	0.174	0.035	0.051	0.007	−0.105	0.023
57	0.364	−0.155	0.198	−0.008	0.122	0.015	−0.083	0.096
58	0.336	−0.078	0.195	0.003	0.133	0.015	−0.115	0.059
59	0.355	−0.101	0.058	−0.051	0.141	0.019	−0.049	0.046
60	0.289	−0.107	0.148	0.009	0.106	0.015	−0.069	0.056
61	0.277	−0.076	0.094	0.006	0.100	−0.004	−0.037	0.037
62	0.298	−0.099	0.078	−0.012	0.095	0.007	−0.071	0.067
63	0.279	−0.055	0.160	−0.010	0.080	0.019	−0.067	0.026
64	0.354	−0.063	0.227	0.048	0.093	0.001	−0.122	0.022
Average all frames	0.333	−0.099	0.143	0.000	0.117	0.013	−0.076	0.051
Standard deviation	0.043	0.038	0.060	0.026	0.046	0.012	0.028	0.025
Standard of the mean	0.014	0.012	0.019	0.008	0.014	0.004	0.009	0.008
Average frames 54–58	0.363	−0.118	0.161	0.003	0.135	0.018	−0.085	0.062
Standard deviation	0.032	0.047	0.058	0.020	0.063	0.014	0.026	0.030
Standard of the mean	0.061	0.024	0.029	0.010	0.031	0.007	0.013	0.015
Average frames 59–64	0.309	−0.084	0.127	−0.001	0.102	0.010	−0.069	0.042
Standard deviation	0.036	0.022	0.063	0.032	0.021	0.009	0.029	0.018
Standard of the mean	0.016	0.010	0.028	0.014	0.009	0.004	0.013	0.008
Difference frames (54-58) − (59-64)	0.054	−0.035	0.033	0.004	0.033	0.008	−0.016	0.020
Comparison of Series 1 and Series 2								
Series 1 average	0.309	−0.083	0.161	0.002	0.069	0.026	−0.065	0.056
Series 2 average	0.333	−0.099	0.143	0.000	0.117	0.013	−0.076	0.051
Overall average	0.321	−0.091	0.152	0.001	0.-93	0.020	−0.071	0.053

Table 3. First derivatives of low-order Zernike functions.

Function name	x-derivative	y-derivative
Piston	$\frac{\partial J_1}{\partial x} = 0$	$\frac{\partial J_1}{\partial y} = 0$
x-tilt	$\frac{\partial J_2}{\partial x} = 2$	$\frac{\partial J_2}{\partial y} = 0$
y-tilt	$\frac{\partial J_3}{\partial x} = 0$	$\frac{\partial J_3}{\partial y} = 2$
Defocus	$\frac{\partial J_4}{\partial x} = 4 \cdot \sqrt{3} \cdot x$	$\frac{\partial J_4}{\partial y} = 4 \cdot \sqrt{3} \cdot y$
X-astigmatism	$\frac{\partial J_5}{\partial x} = 2 \cdot \sqrt{6} \cdot y$	$\frac{\partial J_5}{\partial y} = 4 \cdot \sqrt{6} \cdot x$
T-astigmatism	$\frac{\partial J_6}{\partial x} = -4 \cdot \sqrt{6} \cdot x$	$\frac{\partial J_6}{\partial y} = 2 \cdot \sqrt{6} \cdot y$
x-coma	$\frac{\partial J_7}{\partial x} = 12 \cdot \sqrt{2} \cdot x \cdot y$	$\frac{\partial J_7}{\partial y} = 18 \cdot \sqrt{2} \cdot y^2 + 6 \cdot \sqrt{2} \cdot x^2 - 4 \cdot \sqrt{2}$
y-coma	$\frac{\partial J_8}{\partial x} = 18 \cdot \sqrt{2} \cdot x^2 + 6 \cdot \sqrt{2} \cdot y^2 - 4 \cdot \sqrt{2}$	$\frac{\partial J_8}{\partial y} = 12 \cdot \sqrt{2} \cdot x \cdot y$

$$\chi_x^2 = \sum_{i=1}^{N_{obs}} (SX_i - \Psi_{i,x})^2$$

$$\chi_y^2 = \sum_{i=1}^{N_{obs}} (SY_i - \Psi_{i,y})^2$$

The standard least-squares solution [5] is then given in rms waves at 633 nm by the transformation

$$[a_k] = [MX_{k,j}]^{-1} \cdot [QX_j] \cdot \frac{D}{2 \cdot \lambda_{HeNe}}$$

$$[b_k] = [MY_{k,j}]^{-1} \cdot [QY_j] \cdot \frac{D}{2 \cdot \lambda_{HeNe}}$$

where $D = 1$ meter is the telescope aperture diameter. The measurement vectors QX and QY have the components

$$QX_j = \sum_{i=1}^{N_{obs}} \Psi X_i \cdot \frac{\partial J_j(x_i, y_i)}{\partial x}$$

$$QY_j = \sum_{i=1}^{N_{obs}} \Psi Y_i \cdot \frac{\partial J_j(x_i, y_i)}{\partial y}$$

The matrix to be inverted is given by

$$[MX_{k,j}] = \sum_{i=1}^{N_{obs}} \frac{\partial J_k(x_i, y_i)}{\partial x} \cdot \frac{\partial J_j(x_i, y_i)}{\partial x}$$

$$[MY_{k,j}] = \sum_{i=1}^{N_{obs}} \frac{\partial J_k(x_i, y_i)}{\partial y} \cdot \frac{\partial J_j(x_i, y_i)}{\partial y}$$

Except for measuring errors, the x- and y-components of the slope error vectors are generally not linearly independent. For this reason, the least-squares analysis given in the foregoing must be formulated and solved separately for the x- and y-components, omitting, in each formulation, terms for which the Zernike functional derivatives are identically zero. In the case of symmetrical aberrations, such as defocus, the difference between the x- and y-solutions (which in principle should be identical) gives an estimate of the accuracy of the solution. It should be noted that, whereas Zernike functions are (by design) orthonormal by integration over the unit circle, they are not orthonormal on a finite set of points defined by a Hartmann mask (in this case having 20 holes). Some cross talk between Zernike terms therefore may be expected.

VI. Results

The results of our Zernike wavefront aberration analysis are presented in Table 1 (for data Series 1) and Table 2 (for data Series 2). Geometrical rms spot radii, expressed in arcseconds, are given in column 2. Wavefront aberration coefficients (expressed in waves at 633 nm) for the seven Zernike aberrations considered in our analysis are summarized in columns 3 through 9 of the tables. The coefficients for defocus, X- and T-astigmatism, and x- and y-coma also are plotted against frame number (essentially a function of the time of observation) for convenient intercomparison in Figs. 4 and 5.

From Tables 1 and 2, it is apparent that there are small, but not insignificant, frame-to-frame differences in the magnitudes of the aberrations reported. These variations can be attributed in part to random measuring errors in our determination of spot centroids. However, the largest contributor to the observed variation appears to be slowly varying atmospheric refraction that is not fully averaged out over the duration of a 60-second exposure. The effects are visible in our data at two levels: (1) full-aperture frame-to-frame image motion as measured by excursions of the frame centroid (the mean position of all 20 spots in a frame), as illustrated in Fig. 6, and (2) sub-aperture frame-to-frame spot motions relative to the frame centroid. These movements are significantly larger than our estimated measuring errors. Thus, it must be said that, although the use of time exposures greatly reduces the residual effects of atmospheric turbulence, measurable image motions remain whose time scales are evidently longer than 60 seconds. Although having insufficient data for a conclusive explanation, we suspect slowly varying local patterns of nonuniform atmospheric density ("dome seeing") as the likely cause.

Mean aberration values and standard deviations are tabulated frame by frame in Tables 1 and 2. These statistics are calculated in two ways. First, the mean and standard deviation of all the frames of a series are given. Second, each series is considered in two halves. Thus, in Series 1, frames 39 through 44 are considered as a group, while frames 45 through 50 are considered as a second group. From examination of these results, it is evident that the mean values and standard deviations of these subsets are not significantly different from each other or from each series as a whole; and indeed all four data subsets give similar results. This finding suggests that the observed deviations are indeed sufficiently random that averaging of the data sets for each aberration is in fact meaningful.

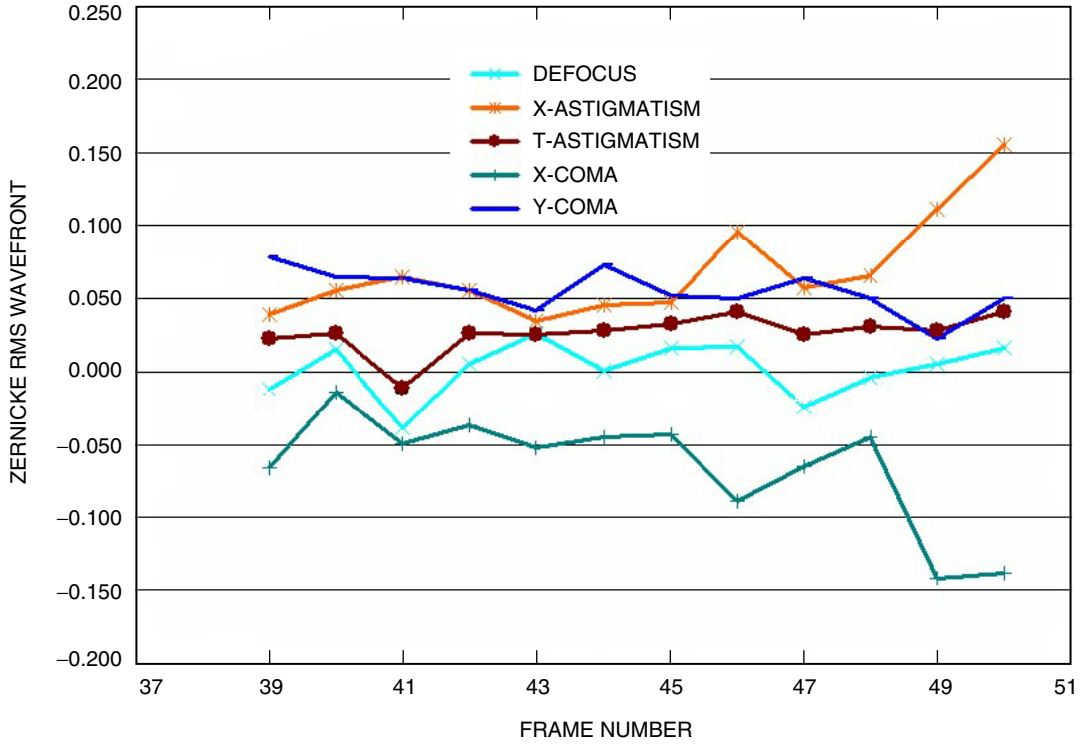

Fig. 4. Depiction of Zernike wavefront aberration coefficients derived from frames 39 through 50 (Series 1). The vertical axis represents Zernike wavefront aberration coefficients in waves at 633 nm. Specific aberrations are identified in the legend. The value of the defocus distance Δ used in the Hartmann computation for this data series was chosed to minimize the average value of the Zernike defocus coefficient for the series. Since wavefront tilt terms are of no importance in estimating image quality, they are omitted from the diagram.

VII. Discussion

In almost every frame, the smallest aberration we measured (other than tilt and defocus) is T-astigmatism, having mean values of 0.020, 0.033, 0.018, and 0.010 wave in the four half-sets of data, and an overall mean of 0.020 wave. The average standard deviation among the 22 individual frames is 0.0125 wave. Such apparently well-behaved statistics suggest that a meaningful standard deviation of the mean might be given by dividing 0.0125 wave by $\sqrt{(N_{obs}-1)}$, yielding a formal probable error of 0.003 wave. While this is perhaps overly optimistic, it is apparent that the precision of order 0.01 wave found in comparisons among individual frames is commensurate with our expectations based on analysis of computer-simulated Hartmann test data, and in fact considerably better than the consistency achieved in factory acceptance tests of the OCTL telescope using interferometry.

In almost every frame, the largest aberration we measured is X-astigmatism, having mean values of 0.049, 0.089, 0.135, and 0.102 wave in the four half-sets of data, and an overall mean of 0.093 wave. The average standard deviation among the 22 individual frames is 0.047 wave, about half the mean value. From Figs. 4 and 5, it is apparent that X-astigmatism is the least well-behaved of the measured aberrations.

From examination of Figs. 4 and 5, it is evident that the five aberrations shown, despite significant frame-to-frame variations, tend to maintain their relative magnitudes (and signs) for the entire set of measurements. Thus, defocus and T-astigmatism remain close to zero, X-astigmatism holds the lead at

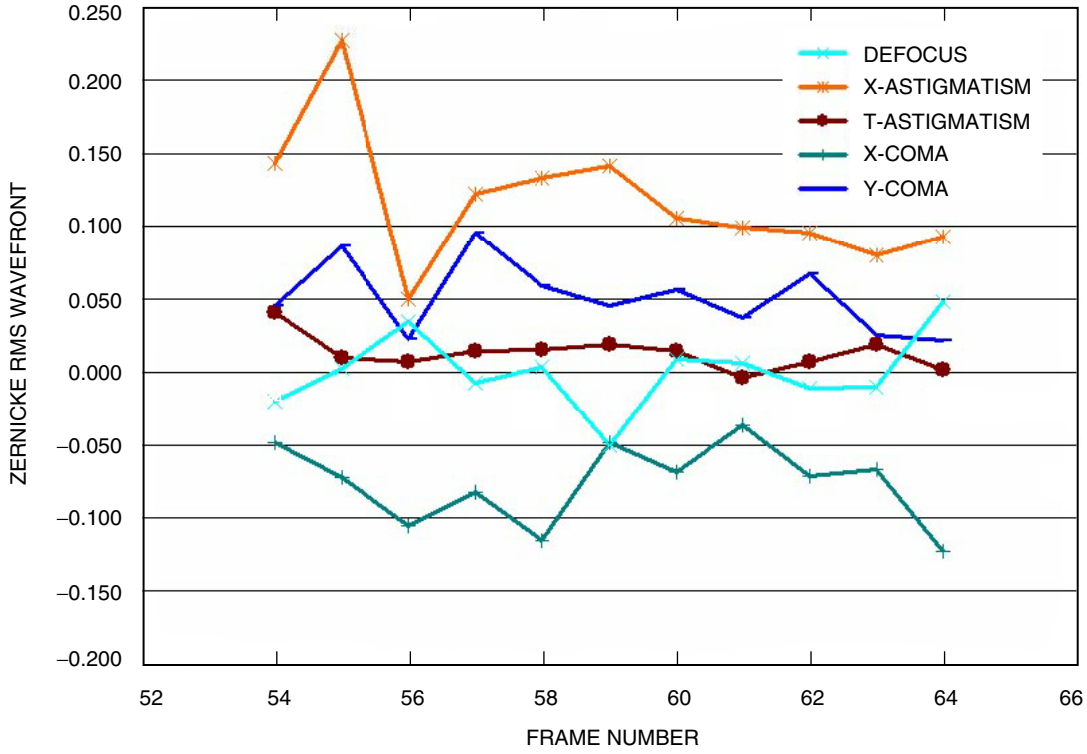

Fig. 5. Continuation of Fig. 4, depicting the Zernike wavefront aberrations derived from frames 54 through 64 (Series 2). The meanings of symbols used are the same as in Fig. 4. As with Series 1, the value of Δ used for Series 2 was chosen to reduce the average Zernike defocus coefficient to a small value.

close to +0.1 wave, while y-coma remains at about +0.05 wave and x-coma almost matches X-astigmatism but in the opposite sign, in the range from −0.05 to −0.1 wave. The results altogether indicate that the overall rss wavefront aberration of the OCTL telescope (ignoring tilt and defocus but considering astigmatism and coma) is around 0.130 wave, or about 2.6 times larger than specified as a performance requirement for the telescope system.

Our results indicate the presence of discernible levels of coma, which could in principle be corrected by a small lateral adjustment of the secondary mirror centration (shifting it by about two thousandths of an inch, or 50 μm, in an appropriate direction). Such an adjustment was not performed because the coma is very small and easily correctable by adaptive optics.

A possible source of systematic error that might introduce spurious aberrations in our test results would arise from errors in the locations of holes in the Hartmann mask. Mask metrology, mentioned earlier (Section II), shows the presence of differential mask shrinkage of about 0.26 percent in the y-direction relative to the x-direction. Our analysis indicates that this could produce, at most, a spurious indication of astigmatism of about 0.007 wave at 633 nm (of undetermined orientation) in the test results reported in this article. Our conclusions are not affected by a possible system error of this magnitude.

The levels of astigmatism and coma reported here are somewhat greater than the levels indicated by acceptance tests performed interferometrically at the factory prior to delivery of the OCTL telescope to Table Mountain. A number of factors might account for this difference, among them (1) the fact that, because of mechanical interference with the test facility at the factory, the acquisition telescope (its weight a source of secondary mirror misalignment) was not attached to the main telescope during vertical line-of-sight tests at the factory; (2) in factory tests, the telescope was fully shrouded against air currents,

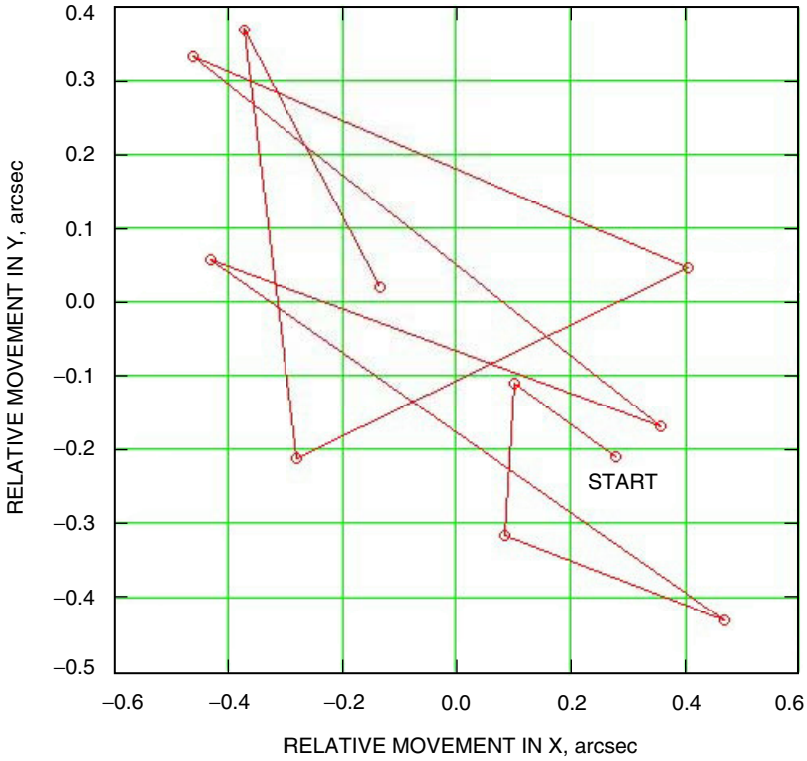

Fig. 6. Observed motion of the spot pattern center of gravity between successive 1-minute exposures in the data of Series 2. The coordinates are in arcsecond units. The overall rms radius of the random walk pattern is 0.42 arcsecond. These motions were removed from the data prior to solving for Zernike wavefront coefficients. Such full-aperture motions would show up as image blur in a long exposure, unless corrected by the tip/tilt element in an adaptive optic system.

whereas it is exposed to "dome seeing" at Table Mountain, as already noted; and (3) following initial delivery, the primary mirror in its cell was removed from the telescope and returned to the factory for rework prior to re-installation and realignment (without benefit of optimal tests for coma) for the tests reported here.

Acknowledgments

In drafting explanatory sections of this article, we have not hesitated to borrow, when appropriate, from an earlier JPL paper co-authored by one of us [2] on a similar application of the technique. We thank Janet Wu of JPL for helpful suggestions on computational methods for spot centroiding, and Vachik Garkanian of JPL for arranging timely fabrication and certification of the Hartmann mask to our dimensional specifications. We are grateful to Dr. Keith Wilson of JPL for facilitating this work and providing helpful suggestions during preparation of this article.

References

[1] J. F. Hartmann, "Objektivunterschungen," *Zeitschrif Instrumentenkd.*, vol. 24, p. 257, 1904; see also D. Malacara, A. Cornejo, and M. V. R. K. Murty, "Biography of Various Optical Testing Methods," *Applied Optics*, vol. 14, pp. 1065–1080, 1975.

[2] A. H. Vaughan and R. P. Korechoff, "Optical Metrology of the Hubble Space Telescope Simulator by Means of Hartmann Tests," *SPIE Conference on Optical Alignment IV*, M. C. Ruda, ed., SPIE Proceedings, vol. 1996, pp. 186–192, ISBN: 0-8194-1245-7, San Diego, California, July 16, 1993. (This work made use of Hartmann procedures developed by Ira S. Bowen for testing the Palomar 5-meter telescope in 1948 and later used by Vaughan and others, in collaboration with Bowen, for testing during fabrication and commissioning of the Palomar 1.5-meter and Las Campanas 2.54-meter telescopes in the 1970s.)

[3] ZEMAX is a proprietary optical design program produced and sold by Focus Software of Tucson, Arizona.

[4] For a comprehensive discussion of image centroiding methods, see P. B. Stetson, "The Techniques of Least Squares and Stellar Photometry with CCDs," http://nedwww/ipac.caltech.edu/level5/Stetson.

[5] W. H. Press, B. P. Flannery, S. A. Teukolsky, and W. T. Vetterling, *Numerical Recipes, The Art of Scientific Computing*, New York: Cambridge University Press, 1986.